Radiative feedbacks from stochastic variability in surface temperature and radiative imbalance

Cristian Proistosescu[1], Aaron Donohoe[2], Kyle C. Armour[3,4], Gerard H. Roe[5], Malte F. Stuecker[4,6], Cecilia M. Bitz[4]

[1]Joint Institute for the Study of the Atmosphere and the Ocean, University of Washington, Seattle, Washington, USA
[2]Applied Physics Laboratory, University of Washington, Seattle, Washington, USA
[3]School of Oceanography, University of Washington, Seattle, Washington, USA
[4]Department of Atmospheric Sciences, University of Washington, Seattle, Washington, USA
[5]Department of Earth and Space Sciences, University of Washington, Seattle, Washington, USA
[6]Cooperative Programs for the Advancement of Earth System Science, University Corporation for Atmospheric Research, Boulder, Colorado, USA

Key Points:

- Net interannual radiative feedback is a weighted average of distinct feedbacks associated with distinct modes of variability.
- Feedbacks obtained from interannual variability are distinct from those governing the response to CO_2 forcing.
- Temperature-independent wind-driven air-sea fluxes are a critical forcing for sub-annual temperature variability.

Corresponding author: Cristian Proistosescu, cproist@uw.edu

Abstract

Estimates of radiative feedbacks obtained by regressing fluctuations in top-of-atmosphere (TOA) energy imbalance and surface temperature depend critically on assumptions about the nature of the stochastic forcing and on the sampling interval. Here we develop an energy-balance framework that allows us to model the different contributions of stochastic atmospheric and oceanic forcing on feedback estimates. The contribution of different forcing components are parsed based on their impacts on the covariance structure of temperature and TOA energy fluxes, and the framework is validated in a hierarchy of climate model simulations that span a range of oceanic configurations and reproduce the key features seen in observations. We find that at least three distinct forcing sources, feedbacks, and time scales are needed to explain the full covariance structure. Atmospheric and oceanic forcings drive modes of variability with distinct relationships between near-surface air temperature and TOA radiation, and the net regression-based feedback estimate is found to be a weighted average of the distinct feedbacks associated with each mode. Moreover, the estimated feedback depends on whether surface temperature and TOA energy fluxes are sampled at monthly or annual timescales. The results suggest that regression-based feedback estimates reflect contributions from a combination of stochastic forcings, and should not be interpreted as providing an estimate of the radiative feedback governing the climate response to greenhouse gas forcing.

1 Introduction

Joint observations of the Earth's temperature and energy imbalance allow for a unique opportunity to empirically constrain radiative feedbacks. However, the satellite record of earth's top of the atmosphere (TOA) radiative imbalance is relatively short and prone to calibration and drift errors, thus making estimates of the net imbalance less reliable than estimates of the relatively large stochastic fluctuations [*Stevens and Schwartz*, 2012]. Consequently, significant effort has gone into estimating radiative feedbacks by regressing fluctuations in global-mean TOA radiative imbalance against fluctuations in global mean near-surface air temperature. These estimates of feedbacks associated with natural variability are often interpreted as either providing a direct estimate of climate sensitivity to greenhouse gases [e.g., *Forster and Gregory*, 2006; *Chung et al.*, 2010; *Dessler*, 2010; *Tsushima and Manabe*, 2013; *Donohoe et al.*, 2014; *Zhou et al.*, 2014; *Trenberth et al.*, 2015; *Forster*, 2016]; or used as an emergent constraint on long-term climate response [e.g., *Zhou et al.*, 2015]. For both direct estimates and emergent constraints, the interpretation of feedbacks associated with natural variability, and their applicability to long-term climate change, rests fundamentally on our ability to physically model the rich structure in the covariability of temperature and radiative anomalies[*Klein and Hall*, 2015], present in both models and observations ([*Forster*, 2016] and Fig. 1). However, this ability has yet to be demonstrated.

Several other issues with regression-based feedback estimates have been identified. Regression estimates rely on an often unstated assumption that variability in TOA radiation arises primarily as a response to variability in surface temperature which is, in turn, driven by nonradiative processes. *Spencer and Braswell* [2010, 2011] noted that if unforced TOA radiation itself plays an important role in driving surface temperature variability, then regression-based feedback estimates will be biased towards higher sensitivity – although the importance of unforced radiation anomalies has been challenged on methodological grounds [*Murphy and Forster*, 2010], and on the basis that air-sea heat flux variability, particularly associated with the El-Niño/Southern Oscillation (ENSO), appears to be large relative to radiative variability [*Dessler*, 2011]. Additionally, the net regression-based estimate of feedbacks associated with internal variability depends on the lag at which the regression is performed, and on whether monthly or annual data are used [*Forster*, 2016].

Here we use a stochastic energy balance framework to build an analytically tractable forward model that reproduces the full structure of the coupling between stochastic anomalies in global-mean surface temperature anomalies and net TOA radiative imbalance. One approach to disentangling the drivers of interannual variability is to recognize that atmospheric and oceanic processes should operate at different characteristic time scales, and, perhaps, with different radiative impacts. We model the spectrum, phase, and covariance relationships of both temperature and radiation as seen in a hier-

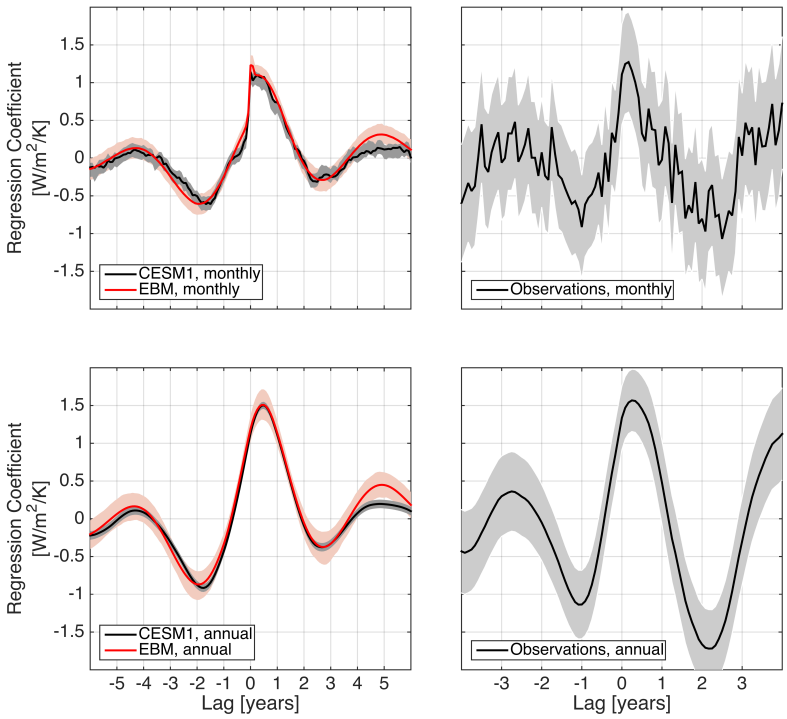

Figure 1. Lagged regressions between global TOA radiation and surface temperature. **A** Monthly anomalies from a 1,800 year long pre-industrial control run of CESM1 (black), and the EBM (red) prediction. Grey shading illustrates 95% regression uncertainty estimates, while pink shading illustrates a 95% uncertainty estimates on EBM regression coefficient based on 1,000 Monte Carlo draws. **B** Observational data sets from 03/2000 to 10/2017. Monthly TOA radiation from CERES [*Wielicki et al.*, 1996], and monthly global mean surface temperature from GISTEMP [*Hansen et al.*, 2010]. Greenhouse gas and aerosol forcing is removed and data is processed as in *Donohoe et al.* [2014]. **C,D** same as **A,B** but for annually averaged anomalies.

archy of general circulation models (GCM) simulations spanning a range of oceanic configurations. This allows us to parse the relative contribution of different stochastic atmospheric and oceanic forcing components, and to interpret the value of the regression-based feedback as a function of the feedbacks elicited by different types of forcing on different time scales.

2 Energy Balance Framework

The classical building blocks for understanding climate variability are simple stochastically forced linear systems. The 1-dimensional version is usually called a *Hasselmann* model [*Hasselmann*, 1976], and has the form

$$C\frac{dT}{dt} = -\lambda T + F, \tag{1}$$

where T here denotes global-mean near-surface air temperature, C denotes heat capacity, λ denotes a radiative feedbacks, and F denotes stochastic forcing. Under a standard assumption of uncorrelated (white noise) forcing, the spectrum of temperature has the familiar Lorentzian shape transitioning from red-noise at high frequencies to white noise at low frequencies (Fig. 2A,B).

The form of the associated equation for TOA radiation depends upon the nature of the forcing [*Forster and Gregory*, 2006; *Spencer and Braswell*, 2010, 2011; *Dessler*, 2011].We first consider the case when forcing, F_1, is due to oceanic heat fluxes. The resulting TOA radiation, Q_1, then depends only on the radiative response to temperature change, T_1, according to

$$Q_1 = -\lambda T_1. \tag{2}$$

If, on the other hand, the system is forced only by stochastic TOA radiative anomalies, such as from cloud variability uncorrelated to T_1, then the forcing, F_2, will directly imprint upon TOA radiation:

$$Q_2 = -\lambda T_2 + F_2 = C\frac{dT_2}{dt}. \tag{3}$$

The two scenarios – oceanic and radiative forcing – can be distinguished through the phase relationships they induce between T and Q. Oceanic forcing leads to direct proportionality between T_1 and Q_1, and thus no phase lag (Fig. 2B). Consequently, the lagged-regression between T_1 and Q_1 is symmetric and equal to λ at lag zero (Fig. 2C). Radiative forcing, however, causes TOA fluxes to be proportional to the rate of change of temperature, leading to a 90° phase lag (Fig. 2E). The lagged-regression then exhibits an anti-symmetric structure with a discontinuity at zero-lag (Fig. 2F).

The third case we consider is that of an ENSO-type process, wherein the associated variability will be quasi-oscillatory, with a peak in the spectrum of the associated temperature variability. Such quasi-oscilatory behavior can be modeled either as a non-linear oscillator [e.g. *Battisti and Hirst*, 1989], or as a stochastically forced linear oscillator [*Thompson and Battisti*, 2000] (Fig. 2G). As ENSO variability is dominated by reorganization of oceanic heat content [*Wyrtki*, 1985; *Jin*, 1997], TOA radiation will be directly proportional to temperature, although we need to account for a possible lag between the peak in temperature and the peak in outgoing TOA radiation [*Xie et al.*, 2016; *Johnson and Birnbaum*, 2017],

$$Q_3(t) = -\lambda T_3(t-\theta). \tag{4}$$

The lagged-regression of temperature and TOA anomalies associated with ENSO variability is a shifted (by phase θ), decaying, quasi-oscillatory function (Fig. 2I). Similar analyses of the lagged-regression symmetry have been used to disentangle forcing versus response relations in analyses of mid-latitude sea-surface temperature variability [e.g., *Frankignoul*, 1985; *von Storch*, 2000; *Bishop et al.*, 2017].

Key to distinguishing each type of forcing are their distinct lagged-regression structures (Fig. 2C,F,I). When all three processes are operating at once, as in the coupled climate system, the net regression-based feedback will be a complex blend of the covariances structure associated with each forcing. We thus turn to GCM simulations to quantify the relative importance of each forcing type, to determine whether they may elicit distinct radiative feedbacks [*Hansen et al.*, 2005; *Winton et al.*, 2010], and to interpret the net feedback obtained by regression.

3 Model Hierarchy

The hierarchy of GCM simulations we employ consists of a set of pre-industrial control simulations of the Community Earth System Model version 1 (CESM1), at 1 degree horizontal resolution, for which long integrations were made available within the Large Ensemble project [Kay et al., 2015]. In order to quantify the roles of the various atmospheric and oceanic forcings in the regression between temperature and TOA radiation, simulations with three distinct types of model configuration are used: a coupled simulation with full ocean dynamics (OCN); a slab ocean simulation (SOM) using the spatially-variable climatological mixed layer-depth from the coupled run; and a fixed sea-surface temperature simulation (fSST), using the climatological SST and sea-ice fields from the coupled run. To ensure commensurate sampling uncertainties, we subset all simulations to a thousand years, equal to the length of the shortest available run (SOM).

The fully-coupled control run of CESM1 reproduces all salient features of the lagged regression structure in the observations (Fig. 1): the relative magnitude of the regression coefficients over a

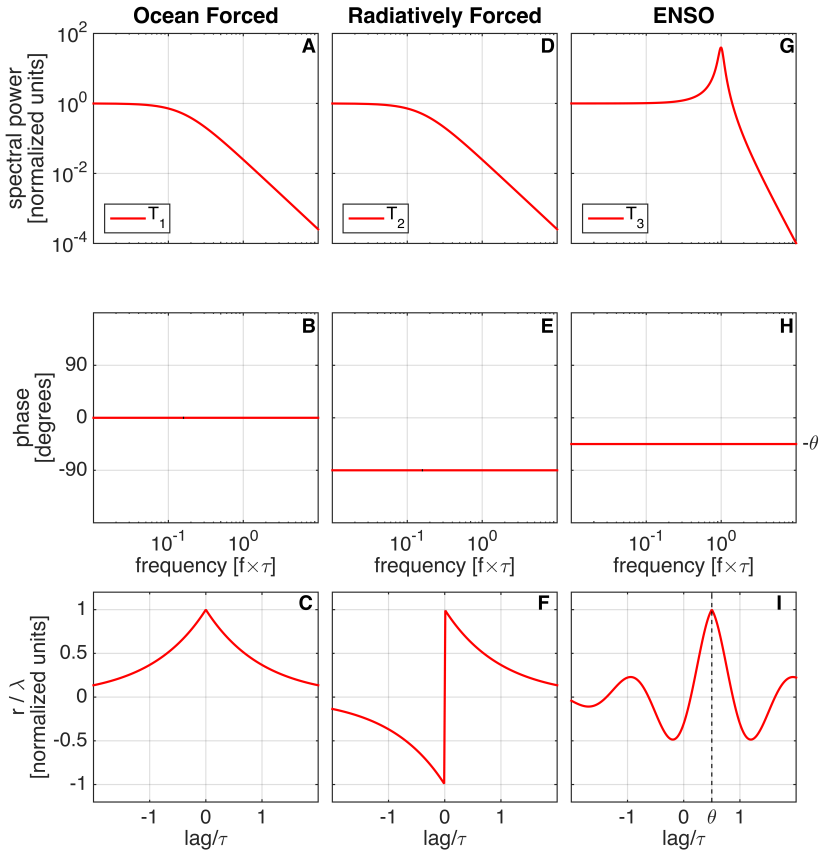

Figure 2. Spectrum, phase difference, and lagged regression of net TOA anomalies, Q, versus global mean temperature, T for the idealized cases presented in section 2. **A-C** depicts the case of a Hasselmann-like model forced by uncorrelated (white noise) oceanic heat fluxes (Eqn. 2); **D-F** depicts a similar Hasselmann-like model, but forced by TOA radiative anomalies (Eqn. 3); while **G-I** depicts an ENSO-like quasi-oscillatory process forced by exchanges between the surface and deep ocean (Eqn. 4).

range of lags using monthly data; the amplification of the zero-lag regression feedback when using annual data; the quasi-sinusoidal structure, the off-set of the maximum covariance towards positive lags, and the sharp jump in regression coefficient around zero. A notable discrepancy is the larger periodicity of the sinusoidal structure in CESM1, attributable to the longer periodicity of CESM1's ENSO cycle compared to the observations. In what follows, we build and tune an energy balance model (EBM) to replicate the regression statistics of each simulation in the CESM1 hierarchy in order to interpret the behavior of the coupled climate system.

3.1 Fixed Sea-Surface Temperature (fSST) Simulation

The spectrum of near-surface air temperature in the fSST simulation (Fig. 3A) has the expected Lorentzian profile, flat at low frequencies and damped at high frequencies. The phase relation between T and Q is centered on zero (Fig. 3B), indicating that the dominant forcing on the atmosphere is provided by heat fluxes from the ocean, rather than from TOA radiative variability. Traditionally, the oceanic source of variance is assumed to be associated with ENSO [*Trenberth et al.*, 2011, 2015; *Dessler*, 2010, 2011, 2013; *Murphy and Forster*, 2010]. However, the fSST simulation does not contain ocean dynamics or ENSO-like SST variability; the source of near-surface air temperature variability is instead provided by stochastic turbulent atmosphere-ocean fluxes.

We thus build on previous two layer models of atmosphere-ocean exchanges [*Barsugli and Battisti*, 1998; *Cronin and Emanuel*, 2013], and consider an atmosphere, with temperature T_a and heat-capacity C_a, coupled to a surface ocean mixed layer, with temperature T_o and heat capacity C_o. Due to its small heat capacity, the land is assumed to be in equilibrium with the atmosphere on monthly time scales. Heat fluxes at the air-sea interface depend on wind speed and on atmosphere-ocean gradients in temperature and humidity. For small perturbations around a steady state, humidity anomalies can be linearized and approximated as proportional to temperature anomalies. The net atmosphere-ocean fluxes can thus be approximated as $\mathcal{H} \propto U(T_a - T_o)$ [e.g. *Hartmann*, 2015]. Ignoring second order terms, anomalous air-sea fluxes can be decomposed to yield two terms: (i) a damping term, $\lambda_{\rm ao}(T_a - T_o) \propto \overline{U}(T_a - T_o)$, proportional to the climatological time-mean wind-speed, $\overline{U}$, and temperature gradient anomalies; and (ii) a stochastic forcing term $F_{\rm ao} \propto U\overline{(T_a - T_o)}$, proportional to surface wind variability and the time-mean temperature gradient. The turbulent feedback $\lambda_{\rm ao}$, is typically an order of magnitude larger than the radiative feedbacks term, denoted $\lambda_{\rm rad,a}T_a$ and $\lambda_{\rm rad,o}T_o$ [*Barsugli and Battisti*, 1998; *Cronin and Emanuel*, 2013]. The different radiative feedbacks $\lambda_{\rm rad,a}$ and $\lambda_{\rm rad,o}$ account for different radiative responses associated with land-atmosphere variability and mixed-layer variability, as well as for radiation emitted by the surface ocean that is not absorbed by the atmosphere. Finally, we consider stochastic radiative anomalies uncorrelated with surface temperature over both land and ocean, $F_{\rm rad} = F_{\rm rad,l} + F_{\rm rad,o}$ and write the full model as:

$$C_a \frac{dT_a}{dt} = -\lambda_{\rm rad,a}T_a - \lambda_{\rm ao}(T_a - T_o) + F_{\rm ao} + F_{\rm rad,l} \quad (5)$$

$$C_o \frac{dT_o}{dt} = -\lambda_{\rm rad,o}T_o + \lambda_{\rm ao}(T_a - T_o) - F_{\rm ao} + F_{\rm rad,o}, \quad (6)$$

$$Q = -\lambda_{\rm rad,a}T_a - \lambda_{\rm rad,o}T_o + F_{\rm rad}. \quad (7)$$

In the fSST configuration, T_o is kept equal to zero. Additionally, the zero phase (Fig. 3B) lag indicating predominant oceanic forcing means that $F_{\rm ao} \gg F_{\rm rad,l}$. This is supported by the fact that the spectrum of TOA fluxes in the CESM1 fSST simulation is two orders of magnitude lower than that of surface heat fluxes at frequencies $f \gg \lambda_{\rm ao}/C_a \gg \lambda_{\rm rad,a}/C_a$, where the forcing terms dominate the feedback terms in Eqn.(5). Denoting $C_1 = C_a\lambda_{\rm rad,a}(\lambda_{\rm rad,a} + \lambda_{ao})^{-1}$, $F_1 = F_{\rm ao}\lambda_{\rm rad,a}(\lambda_{\rm rad,a} + \lambda_{ao})^{-1}$, $\lambda_1 = \lambda_{\rm rad,a}$, and after some reorganization, we can now write a Hasselmann model for the fSST simulation akin to Eqs. (1,2):

$$C_1 \frac{dT_1}{dt} = -\lambda_1 T_1 + F_1, \quad (8)$$

$$Q_1 = -\lambda_1 T_1 + F_{\rm rad},, \quad (9)$$

with $\tau_1 = C_1/\lambda_1 = 0.05$ yrs, and $\lambda_1 = 1.2\mathrm{Wm}^{-2}\mathrm{K}^{-1}$, as fit to the fSST simulation (Appendix).

Since T_1 is forced by atmosphere-ocean fluxes, the radiative term is not correlated with temperature, and its presence in Eqn. (9) introduces uncertainty in the phase relation (Fig. 3B) without altering the zero-mean. The predicted lagged-regression matches the fSST simulation (Fig. 3C), and is consistent with an oceanic source of variance (Fig. 2C). Thus, air temperature variability driven by surface fluxes shows a lag-zero regression of 1.2 $\mathrm{Wm^{-2}K^{-1}}$.

3.2 Slab Ocean Model (SOM) Simulation

We next consider the slab ocean simulation, in which the atmosphere is coupled to a mixed layer ocean in which SSTs are allowed to evolve thermodynamically, but no ocean dynamics are represented. The spectrum of near-surface air temperature (Fig. 3D) has two distinct regimes: one at high frequencies that is consistent with the spectrum of the fSST simulation, and one at frequencies lower than the atmospheric adjustment timescale, indicative of an additional linear mode of variability, T_2, active on multi-year timescales.

The phase relation between TOA anomalies and temperature (Fig. 3E) goes from zero at high frequencies, consistent with the fSST simulation, to 90° on inter-annual time scales where the second mode dominates the variability, indicating a radiative source of variance for T_2 (compare with Fig. 2E). Indeed, since this mode arises on time scales longer than the equilibration time of the atmosphere ($\tau_1 = 0.05$ yrs), the atmosphere and ocean layer will be in equilibrium with one another. On these time scales, we can approximate $T_2 \approx T_a \approx T_o$ and sum Eqs.(5,6) cancelling the F_{ao} terms. This slower mode, T_2, then represents the evolution of the joint atmosphere-mixed layer primarily driven by radiative TOA perturbations. Denoting $C_2 = C_a + C_o$, $\lambda_2 = \lambda_{\mathrm{rad,a}} + \lambda_{\mathrm{rad,o}}$, $F_2 = F_{\mathrm{rad}}$, the Hasselmann model for the second mode can be written akin to Eqs.(1,3) as:

$$C_2 \frac{dT_2}{dt} = -\lambda_2 T_2 + F_{\mathrm{rad}}, \tag{10}$$

$$Q_2 = -\lambda_2 T_2 + F_{\mathrm{rad}}, \tag{11}$$

with $\tau_2 = C_2/\lambda_2 = 2$ yrs and $\lambda_2 = 0.9$ $\mathrm{Wm^{-2}/K}$, as fit to the SOM simulation.

The full behavior of the SOM simulation is thus modeled as the sum of the responses of the surface-flux driven mode, T_1, and the radiative driven mode, T_2. These two modes, as described by Eqs. (8-11), are a good approximation to the actual eigenmodes of the coupled system (Eqs. 5-6), since $\tau_2 \gg \tau_1$ and $\lambda_{\mathrm{ao}} \gg \lambda_{\mathrm{rad}}$ [*Cronin and Emanuel*, 2013]. Both the phase and the lagged-regression predicted by $T_1 + T_2$ match the SOM simulation (Figs. 3E and 3F), and are consistent with a combination of ocean and radiatively forced modes (Figs. 2B,E and 2C,F). The lagged-regression structure shows both the narrow peak at zero-lag associated with ocean-forced T_1 as well as a discontinuity at zero associated with a radiatively-forced mode. Notably, the height of the zero-lag peak for the SOM simulation is lower than the the height of the peak in the fSST simulation, where it is equal to λ_1.

3.3 Coupled Model with Full Ocean Dynamics (OCN)

The fully-coupled simulation includes the same physics described above, but also permits coupled ocean-atmosphere dynamics that give rise to quasi-oscillatory interannual variability, primarily in the form of an ENSO mode of variability. This variability is identifiable by the narrow-band concentration of power in the spectral peak centered on a frequency of $f_E = 1/4.5$ yrs (Fig. 3G). Since an oscillatory solution in a linear model requires at least two eigenmodes, we model the additional ENSO variability as a stochastically forced damped harmonic oscillator [*Thompson and Battisti*, 2000, 2001]. We further allow that the peak in TOA fluxes through an ENSO cycle lags surface temperatures [*Xie et al.*, 2016; *Johnson and Birnbaum*, 2017], such that the response of the third mode becomes:

$$\frac{1}{\omega_E^2}\frac{d^2T_3}{dt^2} + \frac{2}{\tau_3\omega_E^2}\frac{dT_3}{dt} + T_3 = \eta, \tag{12}$$

$$Q_3(t) = \lambda_3 \cdot T_3(t-\theta), \tag{13}$$

where η is a white noise stochastic driving force [*Thompson and Battisti*, 2001]; $\omega_E = 2\pi f_E$ is the resonant angular frequency of the oscillator, $\tau_3 = 4$ yrs is a damping time that controls the width of the peak, $\theta = 8$ months is the lag of radiation relative to temperature, and $\lambda_3 = 3.0$ Wm^{-2}K^{-1} is the radiative feedback of ENSO-related global temperature variability.

Temperature and TOA variability in the fully-coupled simulation (OCN) are modeled as $\sum T_j$, and $\sum Q_j$. Consistent with the CESM1 control simulation (Fig. 3J), relative phase goes as $\phi = \omega\theta \approx 53°$ at the resonant frequency. The lagged-regression structure predicted by $\sum T_j$, and $\sum Q_j$ match the OCN simulation (Fig. 3I) and is consistent with a combination of the three idealized modes (Figs. 2B,E,H and 2C,F,I) operating at once.

4 Regression coefficients and radiative feedbacks

Having assembled a full conceptual model that reproduces the spectral characteristics of the GCM, we are now in a position to understand the full structure of the lagged-regression (Fig. 1), and why it depends on both lag and sampling interval. The lagged regression is equal to the superposition of the distinct feedbacks associated with each mode, weighted by each mode's relative temperature variance and its autocorrelation (see Appendix for derivation):

$$r\,(\text{lag}) = \sum_j \lambda_j \left(\frac{\sigma^2_{T_j}}{\sigma^2_{T_{\text{total}}}} \right) \rho_j(\text{lag}), \tag{14}$$

where $\sigma^2_{T_j} = \text{var}\left(T_j\right)$ is the total variance of mode T_j and $\rho_j(t)$ its autocorrelation function. The regression values at zero lag, and at the ENSO lag θ can be well-approximated as:

$$r\,(0) \approx \lambda_1 \left(\frac{\sigma^2_{T_1}}{\sigma^2_{T_{\text{total}}}} \right) + \lambda_3 \left(\frac{\sigma^2_{T_3}}{\sigma^2_{T_{\text{total}}}} \right) \left[e^{-\theta/\tau_3} \cos\left(\omega_E \theta\right) \right], \tag{15}$$

$$r\,(\theta) \approx \lambda_2 \left(\frac{\sigma^2_{T_2}}{\sigma^2_{T_{\text{total}}}} \right) \left[e^{-\theta/\tau_2} \right] + \lambda_3 \left(\frac{\sigma^2_{T_3}}{\sigma^2_{T_{\text{total}}}} \right). \tag{16}$$

For CESM1, the standard deviations for monthly samples are $\sigma_{T_1} = 0.10, \sigma_{T_2} = 0.08, \sigma_{T_3} = 0.07$ K, the feedback parameters are $\lambda_1 = 1.2, \lambda_2 = 0.9, \lambda_3 = 3.0$ Wm^{-2}K^{-1}, and net regresion-feedbacks are $r(0) = 1.2$ Wm^{-2}K^{-1} and $r(\theta)$=1.0 Wm^{-2}K^{-1}. We repeat our analysis by performing integrations of the same model hierarchy within an earlier version of the GCM, the Community Climate System Model version 4 (CCSM4; [*Gent et al.*, 2011; *Bitz et al.*, 2012]). Within CCSM4, the variance is partitioned differently between the three modes, with ENSO now the dominant mode. Standard deviations are $\sigma_{T_1} = 0.10, \sigma_{T_2} = 0.08, \sigma_{T_3} = 0.13$ K, the feedback parameters are $\lambda_1 = 1.5, \lambda_2 = 1.5, \lambda_3 = 2.2$ Wm^{-2}K^{-1}. The net regression feedbacks are $r(0) = 1.2, r(\theta) = 1.1$ Wm^{-2}K^{-1}, nearly identical to CESM1, despite the significant differences in the feedbacks and relative variances of each mode.

Eqs. (14-16) provide insight into how and why net regression feedback estimates depend on both lag and sampling interval. At zero lag, the auto-correlation of the second, radiatively-forced mode, $\rho_2(0)$ is zero , but T_2 still contributes to the total temperature variance. This presence of additional variance in the predictor variable T that is not manifested in the regressed variable Q is called regression dilution [*Fuller*, 2009], and biases the net feedback low relative to a scenario where all variability in T projects identically on Q. Furthermore, ENSO variability contributes fully to the temperature variance through $\sigma^2_{T_3}$, but its contribution to the covariance of T and Q at zero-lag is damped due to the lag θ . The lagged regression at the ENSO lag θ suffers from similar issues. The first mode, forced by surface fluxes, contributes to the temperature variance, but not to the covariance, since $\theta \gg \tau_1$ and $\rho_1(\theta) \approx 0$, leading to regression dilution. The bias is enhanced by the fact that the contribution of T_2 is also damped by a factor of $e^{-\theta/\tau_2}$ (Eqn. 16).

The different correlation time scales τ_j of the different components means that smoothing (from monthly to annual), does not affect all modes equally. Thus, the ratio of $\sigma_{T_j} / \sum \sigma_{T_k}$ is a function of

sampling interval, leading to different net regression estimates from monthly and from annual data. Using annual averages most strongly suppresses the first mode of variability, such that in CESM1 σ_{T_1} drops from 0.10 to 0.02 K on annual time scales, while σ_{T_2} changes only slightly from 0.09 to 0.08 K, as does σ_{T_3} from 0.08 to 0.07 K. Thus, the regression dilution effect of the surface-flux forced mode is greatly reduced with annual sampling, leading to a larger value of the regression coefficient, as observed by *Forster* [2016] and seen in Fig. 1.

5 Discussion

We find that natural variability in temperature and radiative anomalies is not dominated by a single source of forcing. Rather, variability arises in response to different forcing components exciting different radiative responses. Our results highlight the critical importance of high-frequency variability associated with wind-forced air-sea fluxes. Consistent with previous studies suggesting a dominant ocean-source for the forcing [*Murphy and Forster*, 2010; *Dessler*, 2011], 70% and 81% of the near-surface air temperature variance is attributable to oceanic forcing in CESM1 and CCSM4, respectively. However, this is the result of two independent modes, with no single dominant mode, such that the regression-based estimate of the net feedback is an amalgamation of several mechanisms with different feedbacks, time scales and lags. In all likelihood other modes of variability may be present in the real climate system.

We find the regression-based estimate of the net feedback to be a poor analog for the equilibrium feedback in response to CO_2 forcing, even in a perfect model setup. For CESM1 the feedback in response to CO_2 forcing is $\lambda_{CO_2} = 0.9$ $Wm^{-2}K^{-1}$ [*Meehl et al.*, 2013], compared to $r(0) = 1.2$ and $r(\theta) = 1.1$ $Wm^{-2}K^{-1}$. For CCSM4, $\lambda_{CO_2} = 1.25$ $Wm^{-2}K^{-1}$ [*Bitz et al.*, 2012], nearly 40% larger, despite regression-based estimates of interannual feedback of $r(0) = 1.2$ and $r(\theta) = 1.0$ $Wm^{-2}K^{-1}$, nearly identical to CESM1. The nearly identical values of $\rho(0)$ and $\rho(\theta)$ in the two models arise through compensations in the values of variances and feedbacks of the individual modes. In particular, the ENSO mode, T_3 has the lowest relative variance in CESM1 (23%), and the highest relative variance in CCSM4 (53%), but the change in relative variance is compensated by the change in the radiative feedback magnitude of λ_3.

These results also have implications for our interpretation of emergent constraints. The inter-model spread in regression-based [e.g., *Zhou et al.*, 2015] or fluctuation-dissipation based [e.g., *Cox et al.*, 2018] estimates of net feedbacks is not simply a function of the radiative processes. The model ensemble-spread will be strongly influenced by the significant ensemble-spread of the variance and time scales associated with different modes of variability [e.g., *Chen et al.*, 2017, for spread in ENSO variability]. Thus, emergent constraints that use a bulk regression-based feedback as their basis should be treated with caution.

One possible path forward is identifying commonalities between the feedbacks associated with individual modes or time scales, and the feedbacks governing long-term warming. However, constraining these modes in the observational record is expected to provide several challenges. A complicating factor in using observational data is that temperature measurements often consist of a blend of air temperature over land and sea-surface temperature over the ocean. This could lead to a sub-sampling of the fast mode. However, this bias could be quantified by using a blended model output that would mimic observational sampling [*Richardson et al.*, 2016], or by only analyzing time scales longer than a year, where sea-surface and air temperature are expected to covary. Using a hierarchy of multi-century GCM simulations allowed us to constrain the model parameters to a high degree of accuracy. However, the large number of total EBM parameters and the relatively short observational record will result in trade-offs between likely parameters values that will need to be carefully quantified. Additionally, while this work highlights the importance of the temporal structure of the coupling between temperature and radiation, each of the modes of variability also has a particular spatial pattern that could prove useful in constraining it. Future work should focus on developing a statistical framework to fit the conceptual model to the short and noisy observational record, and on making use of the spatial structure associated with each temporal mode.

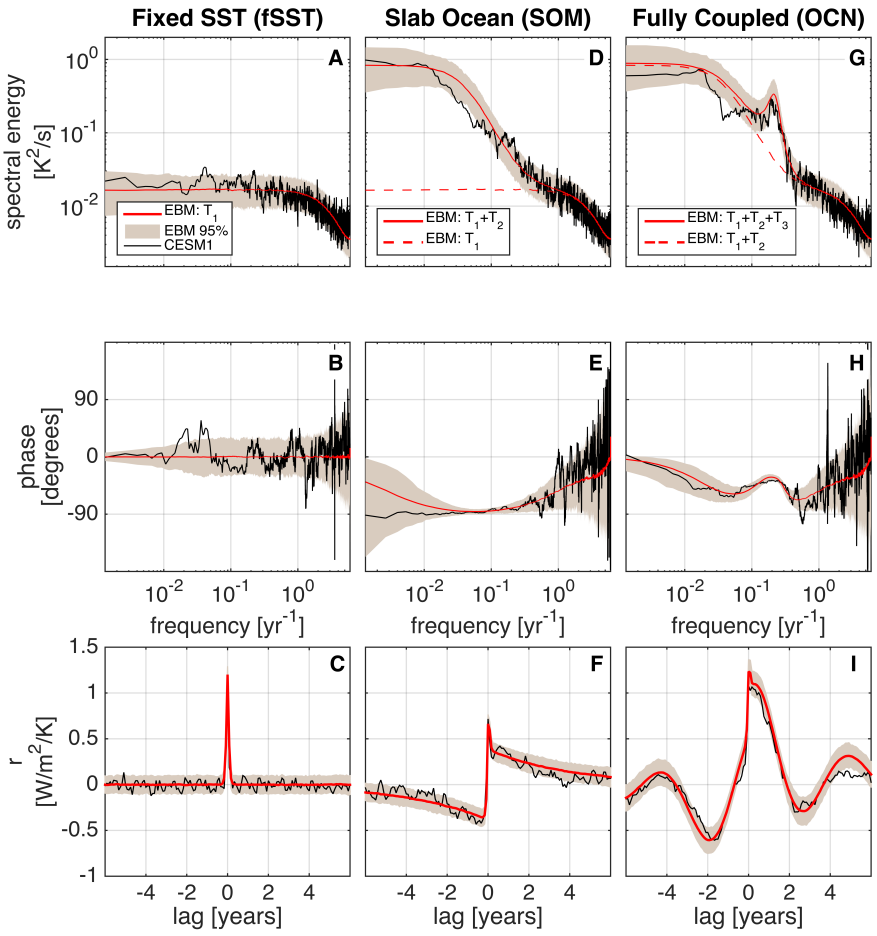

Figure 3. Analytical spectrum, phase difference, and lagged regression coefficient, r, of net TOA anomalies, Q, versus global mean near-surface air temperature, T in a CESM1 control run hierarchy. The hierarchy consists of a fixed SST run (**A-C**), a slab ocean run (**D-F**), as well as the fully coupled control run (**G-I**). The statistics are depicted for CESM1 integrations (black), along with EBM (red) fit. A 95% range of EBM realizations is depicted, based on 1,000 Monte Carlo draws.

A: Analytical Derivations and model fitting

Here we derive analytical solutions to the EBM fit to output from the three CESM1 experiments. For zero-mean processes, the lag-t regression of TOA anomalies relative to temperature anomalies is a ratio of the lagged cross-covariance to the zero-lag temperature auto-covariance,

$$r = \frac{C_{QT}\,(t)}{C_{TT}\,(0)}, \tag{A.1}$$

with the lag-t auto- and cross-covariances, $C_{YX}(t) = \langle Y(t')X(t'+t)\rangle$, computed from the auto- or cross-spectra $S_{YX}(\omega) = \langle Y(\omega)X^*(\omega)\rangle$, using the Wiener-Khinchin theorem as:

$$C_{XY}(t) = \int_{-\infty}^{\infty} S_{XY}(\omega)e^{-i\omega t}\,d\omega. \tag{A.2}$$

Thus, we need to compute the spectrum of temperature, S_{TT} and the cross-spectrum of TOA anomalies and temperature, S_{QT}. The phase lag is computed as the phase of the complex cross-spectrum.

A.1 Fixed Sea-Surface Temperatures (fSST)

Taking the Fourier transform of Eqns. (8,9) and denoting $\tau_1 = C_1/\lambda_1$, $\sigma_{F_1} = \left\langle F_1 F_1^* \right\rangle(\omega)$, and $\sigma_{T_1} = C_{T_1T_1}\,(0)$,

$$\begin{aligned}
i\omega\tau_1\lambda_1 T_1 &= -\lambda_1 T_1 + F_1 && \text{(A.3)}\\
Q_1 &= -\lambda_1 T_1 + F_{\text{rad}} && \text{(A.4)}\\
S_{T_1T_1} &= \frac{\sigma_{F_1}^2}{\lambda_1^2}\frac{1}{1+\omega\tau_1^2} && \text{(A.5)}\\
S_{Q_1T_1} &= \frac{\sigma_{F_1}^2}{\lambda_1^2}\frac{1}{1+\omega\tau_1^2} + \frac{1}{\lambda_1}\frac{\left\langle F_1\cdot F_{\text{rad}}^*\right\rangle}{1+i\omega\tau_1} && \text{(A.6)}
\end{aligned}$$

Using the assumption that $\langle F_1 {F_{\text{rad}}}^*\rangle = 0$,

$$\begin{aligned}
C_{T_1T_1}\,(0) &= \frac{\sigma_{F_1}^2}{\lambda_1^2}\int_{-\infty}^{\infty}\frac{e^{-i\omega t}}{1+\omega^2\tau_1^2}d\omega\bigg|_{t=0} = \frac{1}{\lambda_1^2}\frac{\sigma_{F_1}^2}{\tau_1^2}\sqrt{\frac{\pi}{2}} = \sigma_{T_1}^2 && \text{(A.7)}\\
C_{Q_1T_1}\,(t) &= \frac{\sigma_{F_1}^2}{\lambda_1}\int_{-\infty}^{\infty}\frac{e^{-i\omega t}}{1+\omega^2\tau_2^2}d\omega = \frac{1}{\lambda_1}\frac{\sigma_{F_1}^2}{\tau_1^2}\sqrt{\frac{\pi}{2}}e^{-|t|/\tau} && \text{(A.8)}\\
C_{Q_1T_1}\,(t) &= \lambda_1\sigma_{T_1}e^{-|t|/\tau_1} && \text{(A.9)}\\
r^{(\text{fSST})} &= \lambda_1 e^{-|t|/\tau_1} && \text{(A.10)}
\end{aligned}$$

A.2 Slab Ocean Model (SOM)

Taking the Fourier transform of Eqns. (10,11) and denoting $\tau_2 = C_2/\lambda_2$, $\sigma_{F_2} = \left\langle F_2 F_2^* \right\rangle(\omega)$, and $\sigma_{T_2} = C_{T_2T_2}(0)$,

$$
\begin{aligned}
i\omega\tau_2\lambda_2 T_2 &= -\lambda_2 T_2 + F_2 && \text{(A.11)}\\
Q_2 &= -\lambda_2 T_2 + F_2 = i\omega\tau_2\lambda_2 T_2 && \text{(A.12)}\\
S_{T_2T_2} &= \frac{\sigma_{F_2}^2}{\lambda_2^2}\frac{1}{1+\omega^2\tau_2^2} && \text{(A.13)}\\
S_{Q_2T_2} &= \frac{\sigma_{F_2}^2}{\lambda_2}\frac{i\omega\tau_2}{1+\omega^2\tau_2^2} && \text{(A.14)}\\
C_{T_2T_2}(0) &= \frac{\sigma_{F_2}^2}{\lambda_2^2}\int_{-\infty}^{\infty}\frac{e^{-i\omega t}}{1+\omega^2\tau_2^2}d\omega\bigg|_{t=0} = \frac{1}{\lambda_2^2}\frac{\sigma_{F_2}^2}{\tau_2^2}\sqrt{\frac{\pi}{2}} = \sigma_{T_2}^2 && \text{(A.15)}\\
C_{Q_2T_2}(t) &= \frac{\sigma_{F_2}^2}{\lambda_2}\int_{-\infty}^{\infty}\frac{i\omega e^{-i\omega t}}{1+\omega^2\tau_2^2}d\omega = \frac{1}{\lambda_2}\frac{\sigma_{F_2}^2}{\tau_2^2}\sqrt{\frac{\pi}{2}}e^{-|t|/\tau}\text{sign}(t) && \text{(A.16)}\\
C_{Q_2T_2}(t) &= \lambda_2\sigma_{T_2}e^{-|t|/\tau_2}\text{sign}(t) && \text{(A.17)}
\end{aligned}
$$

Since the modes are assumed independent,

$$
\begin{aligned}
S_{TT}^{(\text{SOM})} &= S_{T_1T_1} + S_{T_2T_2} && \text{(A.18)}\\
S_{QT}^{(\text{SOM})} &= S_{Q_1T_1} + S_{Q_2T_2} && \text{(A.19)}\\
C_{TQ}^{(\text{SOM})} &= C_{Q_1T_1} + C_{Q_2T_2} && \text{(A.20)}\\
C_{TT}^{(\text{SOM})} &= \sigma_{T_1} + \sigma_{T_2} && \text{(A.21)}\\
r^{(\text{SOM})}(t) &= \lambda_1\left(\frac{\sigma_{T_1}^2}{\sigma_{\text{total}}^2}\right)\left(e^{-|t|/\tau_1}\right) + \lambda_2\left(\frac{\sigma_{T_2}^2}{\sigma_{\text{total}}^2}\right)\left(e^{-|t|/\tau_2}\text{sign}(t)\right) && \text{(A.22)}
\end{aligned}
$$

A.3 Coupled run with full ocean dynamics (OCN)

Taking the Fourier transform of Eqns. (12,13), and denoting $\omega_E^* = \omega_E - 1/\tau_3$, $\sigma_\eta^2 = \langle\eta\eta^*\rangle$

$$
\begin{aligned}
-\frac{\omega^2}{\omega_E^2}T_3 + \frac{2i\omega}{\tau_3\omega_E^2}T_3 + T_3 &= \eta && \text{(A.23)}\\
Q_3 &= \lambda_3 T_3 e^{i\omega\theta} && \text{(A.24)}\\
S_{T_3T_3} &= \frac{\sigma_\eta^2}{\left(\omega_E^2-\omega^2\right)^2 + 4\omega^2\tau_3^{-2}} && \text{(A.25)}\\
S_{Q_3T_3} &= \frac{\lambda_3\sigma_\eta^2 e^{i\omega\theta}}{\left(\omega_E^2-\omega^2\right)^2 + 4\omega^2\tau_3^{-2}} && \text{(A.26)}\\
& && \text{(A.27)}
\end{aligned}
$$

The auto- and cross-covariances are [*Wang and Uhlenbeck*, 1945]:

$$
\begin{aligned}
C_{T_3T_3}(0) &= \sigma_\eta^2\omega_E^2\int_{-\infty}^{\infty}\frac{e^{-i\omega t}}{\left(\omega_E^2-\omega^2\right)^2 + 4\omega^2\tau_3^{-2}}d\omega\bigg|_{t=0} && \text{(A.28)}\\
C_{T_3T_3}(0) &= \pi\sigma_\eta^2\omega_E^2 && \text{(A.29)}\\
C_{Q_3T_3}(t) &= \lambda_3\sigma_\eta^2\omega_E^2\int_{-\infty}^{\infty}\frac{e^{-i\omega(t-\theta)}}{\left(\omega_E^2-\omega^2\right)^2 + 4\omega^2\tau_3^{-2}}d\omega && \text{(A.30)}\\
C_{Q_3T_3}(t) &= \lambda_3\pi\sigma_\eta^2\omega_E^2 e^{-|t-\theta|/\tau_3}\left[\cos\left(\omega_E^*(t-\theta)\right) + \frac{1}{\omega_E^*\tau_3}\sin\left(\omega_E^*(t-\theta)\right)\right] && \text{(A.31)}
\end{aligned}
$$

Using the independence of the modes,

$$S_{TT}^{(\mathrm{OCN})} = \sum_{j=1}^{3} S_{T_j T_j} \tag{A.32}$$

$$C_{QT}^{(\mathrm{OCN})} = \sum_{j=1}^{3} C_{Q_j T_j} \tag{A.33}$$

$$r(t) = \sum_{j=}^{3} \lambda_j \frac{\sigma_{T_j}^2}{\sigma_{T_{total}}^2} \rho_j\,(t) \tag{A.34}$$

$$\rho_1\,(t) = e^{-|t|/\tau_1} \tag{A.35}$$

$$\rho_2\,(t) = e^{-|t|/\tau_2} \mathrm{sign}\,(t) \tag{A.36}$$

$$\rho_3\,(t) = e^{-|t-\theta|/\tau_3} \left[\cos\left(\omega_E^*\,(t-\theta)\right) + \frac{1}{\omega_E^* \tau_3} \sin\left(\omega_E^*\,(t-\theta)\right) \right] \tag{A.37}$$

At $t = 0$, $\rho_2\,(0) = 0$. Since $\theta \approx 8$ months, and $\omega_E = 2\pi/5$ rad/years, $\rho_3\,(0)$ wil be dominated by the cosine term.

$$\rho_3\,(0) \approx e^{-\theta/\tau_3} \cos\left(\omega_E^* \theta\right) \tag{A.38}$$

At $t = \theta$ it follows from $\tau_1 \ll \theta$, that $\rho_1\,(\theta) \approx 0$.

A.4 Fitting procedure

Parameters are obtained in the following manner and order. $(\sigma_{F_1}^2 \lambda_1^{-2})$ and τ_1 are obtained by a non-linear least-squares (NLSQ) of Eqn. (A.5) to the periodogram of near-surface air temperature from the fSST simulation (Fig. 3A). λ_1 is obtained using an NLSQ of Eqn. (A.10) to the lagged regression of TOA vs near-surface air temperature in the fSST simulation (Fig. 3C). $(\sigma_{F_2}^2 \lambda_{-2})$ and τ_2 are obtained by NLSQ of Eqn. (A.18) to the periodogram of near-surface air temperature in the SOM simulation (Fig. 3D). λ_2 is obtained using an NLSQ of Eqn. (A.22) to the lagged regression of TOA vs near-surface air temperature in the fSST simulation (Fig. 3F). σ_η^2, ω_E, τ_3 are obtained by NLSQ of Eqn. (A.32) to the periodogram of near-surface air temperature in the OCN simulation(Fig. 3D). λ_3 and θ are obtained using an NLSQ of Eqn. (A.34) to the lagged regression of TOA vs near-surface air temperature in the OCN simulation.

Acknowledgments

We thank David Battisti and Peter Huybers for insightful discussions. CP was supported by a JISAO postdoctoral fellowship. MFS was supported by the NOAA Climate and Global Change Postdoctoral Fellowship Program, administered by UCAR's Cooperative Programs for the Advancement of Earth System Sciences (CPAESS).

References

Barsugli, J. J., and D. S. Battisti (1998), The basic effects of atmosphere–ocean thermal coupling on midlatitude variability, *Journal of the Atmospheric Sciences*, *55*(4), 477–493.

Battisti, D. S., and A. C. Hirst (1989), Interannual variability in a tropical atmosphere–ocean model: Influence of the basic state, ocean geometry and nonlinearity, *Journal of the atmospheric sciences*, *46*(12), 1687–1712.

Bishop, S. P., R. J. Small, F. O. Bryan, and R. A. Tomas (2017), Scale dependence of midlatitude air–sea interaction, *Journal of Climate*, *30*(20), 8207–8221.

Bitz, C. M., K. Shell, P. Gent, D. Bailey, G. Danabasoglu, K. Armour, M. Holland, and J. Kiehl (2012), Climate sensitivity of the Community Climate System Model, version 4, *Journal of Climate*, *25*(9), 3053–3070.

Chen, C., M. A. Cane, A. T. Wittenberg, and D. Chen (2017), ENSO in the CMIP5 simulations: life cycles, diversity, and responses to climate change, *Journal of Climate*, *30*(2), 775–801.

Chung, E.-S., B. J. Soden, and B.-J. Sohn (2010), Revisiting the determination of climate sensitivity from relationships between surface temperature and radiative fluxes, *Geophysical Research Letters*, *37*(10).

Cox, P. M., C. Huntingford, and M. S. Williamson (2018), Emergent constraint on equilibrium climate sensitivity from global temperature variability, *Nature*, *553*(7688), 319.

Cronin, T. W., and K. A. Emanuel (2013), The climate time scale in the approach to radiative-convective equilibrium, *Journal of Advances in Modeling Earth Systems*, *5*(4), 843–849.

Dessler, A. (2013), Observations of climate feedbacks over 2000–10 and comparisons to climate models, *Journal of Climate*, *26*(1), 333–342.

Dessler, A. E. (2010), A determination of the cloud feedback from climate variations over the past decade, *Science*, *330*(6010), 1523–1527.

Dessler, A. E. (2011), Cloud variations and the earth's energy budget, *Geophysical Research Letters*, *38*(19).

Donohoe, A., K. C. Armour, A. G. Pendergrass, and D. S. Battisti (2014), Shortwave and longwave radiative contributions to global warming under increasing CO_2, *Proceedings of the National Academy of Sciences*, *111*(47), 16,700–16,705.

Forster, P. M. (2016), Inference of climate sensitivity from analysis of Earth's energy budget, *Annual Review of Earth and Planetary Sciences*, *44*, 85–106.

Forster, P. M. F., and J. M. Gregory (2006), The climate sensitivity and its components diagnosed from earth radiation budget data, *Journal of Climate*, *19*(1), 39–52.

Frankignoul, C. (1985), Sea surface temperature anomalies, planetary waves, and air-sea feedback in the middle latitudes, *Reviews of geophysics*, *23*(4), 357–390.

Fuller, W. A. (2009), *Measurement error models*, vol. 305, John Wiley & Sons.

Gent, P. R., G. Danabasoglu, L. J. Donner, M. M. Holland, E. C. Hunke, S. R. Jayne, D. M. Lawrence, R. B. Neale, P. J. Rasch, M. Vertenstein, et al. (2011), The Community Climate System Model version 4, *Journal of Climate*, *24*(19), 4973–4991.

Hansen, J., R. Ruedy, M. Sato, and K. Lo (2010), Global surface temperature change, *Reviews of Geophysics*, *48*(4).

Hansen, J. e., M. Sato, R. Ruedy, L. Nazarenko, A. Lacis, G. Schmidt, G. Russell, I. Aleinov, M. Bauer, S. Bauer, et al. (2005), Efficacy of climate forcings, *Journal of Geophysical Research: Atmospheres*, *110*(D18).

Hartmann, D. L. (2015), *Global physical climatology*, vol. 103, Newnes.

Hasselmann, K. (1976), Stochastic climate models part I. theory, *Tellus*, *28*(6), 473–485.

Jin, F.-F. (1997), An equatorial ocean recharge paradigm for ENSO. part I: Conceptual model, *Journal of the atmospheric sciences*, *54*(7), 811–829.

Johnson, G. C., and A. N. Birnbaum (2017), As El Niño builds, pacific warm pool expands, ocean gains more heat, *Geophysical Research Letters*, *44*(1), 438–445.

Klein, S. A., and A. Hall (2015), Emergent constraints for cloud feedbacks, *Current Climate Change Reports*, *1*(4), 276–287.

Meehl, G. A., W. M. Washington, J. M. Arblaster, A. Hu, H. Teng, J. E. Kay, A. Gettelman, D. M. Lawrence, B. M. Sanderson, and W. G. Strand (2013), Climate change projections in CESM1 (CAM5) compared to CCSM4, *Journal of Climate*, *26*(17), 6287–6308.

Murphy, D., and P. Forster (2010), On the accuracy of deriving climate feedback parameters from correlations between surface temperature and outgoing radiation, *Journal of Climate*, *23*(18), 4983–4988.

Richardson, M., K. Cowtan, E. Hawkins, and M. B. Stolpe (2016), Reconciled climate response estimates from climate models and the energy budget of earth, *Nature Climate Change*, *6*(10), 931–935.

Spencer, R. W., and W. D. Braswell (2010), On the diagnosis of radiative feedback in the presence of unknown radiative forcing, *Journal of Geophysical Research: Atmospheres*, *115*(D16).

Spencer, R. W., and W. D. Braswell (2011), On the misdiagnosis of surface temperature feedbacks from variations in Earth's radiant energy balance, *Remote Sensing*, *3*(8), 1603–1613.

Stevens, B., and S. E. Schwartz (2012), Observing and modeling Earth's energy flows, *Surveys in geophysics*, *33*(3-4), 779–816.

Thompson, C., and D. Battisti (2000), A linear stochastic dynamical model of ENSO. part I: Model development, *Journal of Climate*, *13*(15), 2818–2832.

Thompson, C., and D. Battisti (2001), A linear stochastic dynamical model of ENSO. part II: Analysis, *Journal of Climate*, *14*(4), 445–466.

Trenberth, K. E., J. T. Fasullo, and J. P. Abraham (2011), Issues in establishing climate sensitivity in recent studies, *Remote Sensing*, *3*(9), 2051–2056.

Trenberth, K. E., Y. Zhang, J. T. Fasullo, and S. Taguchi (2015), Climate variability and relationships between top-of-atmosphere radiation and temperatures on Earth, *Journal of Geophysical Research: Atmospheres*, *120*(9), 3642–3659.

Tsushima, Y., and S. Manabe (2013), Assessment of radiative feedback in climate models using satellite observations of annual flux variation, *Proceedings of the National Academy of Sciences*, *110*(19), 7568–7573.

von Storch, J.-S. (2000), Signatures of air–sea interactions in a coupled atmosphere–ocean GCM, *Journal of Climate*, *13*(19), 3361–3379.

Wang, M. C., and G. E. Uhlenbeck (1945), On the theory of the brownian motion II, *Reviews of modern physics*, *17*(2-3), 323.

Wielicki, B. A., B. R. Barkstrom, E. F. Harrison, R. B. Lee III, G. Louis Smith, and J. E. Cooper (1996), Clouds and the Earth's Radiant Energy System (CERES): An earth observing system experiment, *Bulletin of the American Meteorological Society*, *77*(5), 853–868.

Winton, M., K. Takahashi, and I. M. Held (2010), Importance of ocean heat uptake efficacy to transient climate change, *Journal of Climate*, *23*(9), 2333–2344.

Wyrtki, K. (1985), Water displacements in the Pacific and the genesis of El Niño cycles, *Journal of Geophysical Research: Oceans*, *90*(C4), 7129–7132.

Xie, S.-P., Y. Kosaka, and Y. M. Okumura (2016), Distinct energy budgets for anthropogenic and natural changes during global warming hiatus, *Nature Geoscience*, *9*(1), 29.

Zhou, C., A. Dessler, M. Zelinka, P. Yang, and T. Wang (2014), Cirrus feedback on interannual climate fluctuations, *Geophysical Research Letters*, *41*(24), 9166–9173.

Zhou, C., M. D. Zelinka, A. E. Dessler, and S. A. Klein (2015), The relationship between interannual and long-term cloud feedbacks, *Geophysical Research Letters*, *42*(23).